

# Eutectic dynamics and control of gold-encapped gallium arsenide nanowires imaged by 4D electron microscopy

Bin Chen,<sup>1,\*</sup> Xuewen Fu,<sup>1</sup> Jau Tang,<sup>1,\*</sup> Mykhaylo Lysevych,<sup>2</sup> Hark Hoe Tan,<sup>3</sup> Chennupati Jagadish,<sup>3</sup>  
Ahmed H. Zewail<sup>1,†</sup>

<sup>1</sup>Physical Biology Center for Ultrafast Science and Technology, Arthur Amos Noyes Laboratory of Chemical Physics, California Institute of Technology, Pasadena, CA 91125, USA

<sup>2</sup>Australian National Fabrication Facility, Research School of Physics and Engineering, The Australian National University, Canberra, ACT 2601, Australia

<sup>3</sup>Department of Electronic Materials Engineering, Research School of Physics and Engineering, The Australian National University, Canberra, ACT 2601, Australia

\*Corresponding author. Email: [bchen5@caltech.edu](mailto:bchen5@caltech.edu), [jautang@caltech.edu](mailto:jautang@caltech.edu)

†Deceased

**Abstract:** A eutectic reaction is a special chemical/physical reaction involving multiple phases, solid or liquid, to form a joint lattice structure with a unique atomic ratio between the components. Visualization of phase reaction of composite nanomaterials with high spatial and temporal resolution provides a key understanding of alloy growth with important industrial applications. However, it has been a rather challenging task. Here we report the direct imaging and control of the phase reaction dynamics of a single, as-grown free-standing gallium arsenide nanowire encapped with a gold nanoparticle, free from environmental confinement or disturbance, using four-dimensional electron microscopy. A laser heating pulse initiates the eutectic reaction at a temperature much lower than the melting points of the composite materials, followed by a precisely time-delayed electron pulse to visualize the transient states of nucleation, growth and solidification of the complex. Combined with theoretical modeling, useful thermodynamic parameters of the newly formed alloy phases and their crystal structures could be determined. This technique of dynamical control and 4D imaging of phase reaction processes on the nanometer-ultrafast time scale open new venues for engineering various reactions in a wide variety of other systems.

**Keywords:** Eutectic reaction, Au/GaAs nanowires, phase reaction, Crystallization, Structural dynamics, 4D electron microscopy

**Main text:**

A eutectic system refers to a unique thermodynamic entity that forms a joint lattice structure with a specific atomic ratio between the constituents. The eutectic temperature describes the lowest temperature at which the mixed substances become fully molten. Comprehensive understanding of eutectic behavior offers a wide variety of applications, including alloys for structural components and eutectic soldering in airplanes and cars<sup>1</sup>, functional electronics in solar energy harvesting<sup>2,3</sup> and eutectic bonding in chips for integrated circuits<sup>4</sup>. Fundamental properties of a solid microstructure from eutectic reactions depend on several factors, for example, the temperature that governs the eutectic reaction and the interfacial nucleation of solid solutions<sup>5,6</sup>.

Eutectic related phenomena have usually been studied via post-processing measurements, and recently visualized by in situ electron microscopy to investigate long time (from seconds to hours) diffusion processes<sup>7-12</sup>. Elucidation of the chemical/physical mechanism underlying those eutectic processes requires time-resolved measurements of the dynamic phase formation. However, probing eutectic reactions in nanostructures is very difficult because of the small sizes and the very short time scales involved, as well as the sensitivity issues to detect those transient processes that occur in non-equilibrium conditions for nanomaterials in a small quantity.

Recent development of 4D electron microscopy (4D-EM) offers direct visualization of the transient behavior of individual nanostructures with high spatiotemporal resolution<sup>13-17</sup>. Here, we report the direct observation and control of the eutectic reaction dynamics in Au/GaAs nanowires (NWs) by 4D-EM (see schematics in Fig. 1a). The eutectic reaction processes of the NWs are induced and controlled by a temperature jump triggered by a laser heating pulse, followed by a delayed photogenerated electron packet to probe the spatiotemporal evolution of the nanostructures. Using single-shot imaging one can observe the transient intermediates of the NW during the reactions. Although the raised temperatures are below

the melting points for the Au bead and the underneath GaAs NW, the observed reduction in NW length and the growth of the bead size are a result of the eutectic reaction between the two. For the time scale, the transient nucleation and growth of the eutectic phases are complete within  $\sim 80$  ns while the morphological changes of the top bead lasts until 100 ns. The observed huge reduction rate of the NW length, which is not a simple diffusion-dominated process, will be discussed. Based on quantitative analysis and theoretical modeling of these measurements, we are able to extract useful thermodynamic parameters of the newly formed alloy phases determined by Bragg diffraction studies, leading to a better understanding of nanoscale phase reactions.

## Results and Discussion

**Experimental implementation.** The difficulty of unambiguously exploring the ultrafast eutectic dynamics of a single Au/GaAs NW lies in isolating the NW from any EM supporting films (e.g., carbon films) while achieving a controllable NW geometry that is accurate enough for data analysis. We overcame this difficulty with a scheme of detecting the NWs that were grown perpendicular to the substrate surface. Namely, by directly putting the as-grown NWs still intact on the GaAs substrate (see Methods) into the 4D-EM (Fig. 1b), one could exclude any sample contamination or possible ambiguity caused by the holding films usually present for normal EM grids. The GaAs substrate was carefully aligned to be parallel to the electron beam so that the free-standing NWs were visible (otherwise, a very slight misalignment or tilting of the substrate, e.g., only  $0.5^\circ$ , would block the electron beam for the probing of NWs since the NWs were only hundreds of nanometers long in the direction vertical to the substrate surface).

For imaging the reaction dynamics from a single NW, the NWs were purposely grown on the substrate with large separation (several microns away from each other), as shown in the projections of the NWs (Fig. 1c). With this large separation among the NWs, the disturbance from any neighboring NW

could be effectively avoided during the experiments. The NW transient morphologies during the eutectic reactions were captured by single-pulse imaging mode of 4D-EM, where an entire image was acquired with only one incident laser pulse followed by one electron pulse (contains  $\sim 10^5$  electrons). For stroboscopic experiments the repetition rate was set at 1 kHz, ensuring the full recovery of the dynamical process. Details of the procedure are given in previous studies from this group<sup>18-20</sup>.

**Morphology and structure of the NW.** Figure 2 shows the typical micrographs and diffraction patterns of the Au/GaAs NWs in stroboscopic mode without the incident pump laser. In the images, the NWs are aligned vertically with respect to the GaAs substrate. A gold nanoparticle is located at the tip of each GaAs NW. The targeted NW has a diameter of 108 nm, and its diffraction pattern (SA-1 region) is presented in the upper rightmost column. The pattern indicates that GaAs has a hexagonal wurtzite (WZ) structure with the growth direction oriented along the  $[000\bar{1}]$  direction. Shown in the inset of the leftmost middle column is a typical microstructure of the NW tip. The diffraction pattern of the tip, corresponding to the SA-2 region, exhibits additional diffraction spots. The unmarked spots are the same as that in the upper diffraction pattern, which come from the WZ GaAs. The marked extra  $\langle 111 \rangle$  ones are from the cubic zinc-blende (ZB) segments of GaAs<sup>21</sup>. This double-spot pattern indicates a twinned ZB component. The small ZB constriction (the dark line marked by an arrow is the ZB/WZ interface) is due to the growth termination procedure<sup>22</sup>.

Tomography was carried out to verify how the NWs behaved during laser excitation (the bottom row of micrographs). It demonstrates that the NWs are straight (without bending) when viewed at different tilting angles. No breakage of the NW was observed either. This experiment ensured unambiguous determination of the shrinkage of the NW length after each single-pulse laser excitation.

**Imaging of eutectic reactions.** To reveal the irreversible eutectic reactions, single-shot imaging methodology was employed. The results of the size changes of the NW are shown in Fig. 3. Initially, the NW has a length of 918 nm (0 laser shot). After a laser pulse at a fluence of 5.5 mJ/cm<sup>2</sup>, the length of the NW became 893 nm, corresponding to a ~3% shrinkage. Compared to the initial NW, there was a 22% length reduction after 23 laser pulses. The NW length (after 46 laser pulses) was finally reduced to 421 nm after the entire run of the experiment, which was associated with a total length shrinkage of 54%. During the whole sequence of laser heating experiments, the choice of the number of pulses and laser fluence (from 5.5 to 40 mJ/cm<sup>2</sup>) was set so that the NW could continue its shrinkage.

Although the NW axial length decreased significantly (Fig. 3, top), no obvious width change of the NW was observed (Supplementary Fig. 1). Only the top bead, namely, the region with darker contrast than the pure GaAs part in the images, increased in size. Further analysis on the NW volume change revealed that the reduction of GaAs volume resulted in the increase of bead volume, causing no obvious change of the total volume (see Supplementary Fig. 2 for the calculations). These results indicate that the GaAs body remained solid phase while the vanished portion of the GaAs reacted with the top bead to form new phases during laser excitation.

**Identification of the formed phases.** Selected-area diffraction studies disclosed the nature of the newly formed phases during the reactions (Supplementary Fig. 3). Compared to the initial components (Fig. 2), new phases of Au<sub>7</sub>Ga<sub>2</sub> and AuGa appeared after the first few laser shots. According to the Au-Ga phase diagram (Supplementary Fig. 4), the Au<sub>7</sub>Ga<sub>2</sub> phase occurs at a temperature as low as 555 K<sup>23</sup>, which is much lower than the melting point of either Au (1337 K) or GaAs (1511 K). As more GaAs was incorporated into the top bead, eutectic phases of AuGa and AuGa<sub>2</sub> were formed. The temperature needed

for this eutectic reaction, liquid  $\rightarrow$  AuGa + AuGa<sub>2</sub>, is 725 K, still much lower than the melting points of the individual components in the initial materials (1337 K for Au and 1511 K for GaAs).

Calculations using two-temperature model for Au and three-temperature model for GaAs show that the lattice temperatures (at a fluence of 5.5 mJ/cm<sup>2</sup>) of the top bead and GaAs body are 566 and 571 K (see Supplementary Information for detailed calculations), respectively, which triggers the reaction to form Au<sub>7</sub>Ga<sub>2</sub> phase. At high fluences, for example, 19.5 mJ/cm<sup>2</sup>, the effective temperature of the top bead is 1196 K, high enough to facilitate the eutectic reactions for the formation of AuGa and AuGa<sub>2</sub> phases. These simulated results are in reasonably good agreement with our experimental observations.

**Thermal properties of the newly formed phases.** Theoretical modeling was employed to calculate the absorbed heat for both the bead and the NW so that the thermal properties for alloy phases during eutectic reactions could be determined (Supplementary Information). Useful parameters, such as the latent heat and specific heat for the newly formed phases, are retrieved and the results are summarized in Table 1. We found that the latent heat of Au<sub>7</sub>Ga<sub>2</sub> and AuGa are 8 and 21 kJ/mol while their specific heat are 62 and 41 J/mol.K, respectively. In comparison, for the initial phases Au and GaAs, the latent heat are 12 and 106 kJ/mol, and the specific heat are 25 and 48 J/mol.K, respectively<sup>24,25</sup>. Because of the presence of latent heat and the lower resultant bead temperature due to increasingly bigger bead size, one needs to increase laser fluences in order to shrink the NW further. Moreover, it is noteworthy that at high fluences (23 mJ/cm<sup>2</sup> or above) the GaAs NW has not melted even though the calculated temperatures (without taking into account the latent heat for melting) are higher than its melting point (Fig. 3). This is because the energy from a laser pulse is not sufficient to overcome the large latent heat of GaAs for its melting.

**Time-resolved dynamics.** To reveal the ultrafast eutectic dynamics, two sets of time-resolved experiments were performed on the NWs. In the stroboscopic dynamics (Fig. 4, top), the time-dependent integrated diffraction intensity at a low fluence of  $3 \text{ mJ/cm}^2$  was plotted to determine the time constant evolution of the non-equilibrium thermodynamics of the NW. It shows a quick decrease after time zero and then a relatively slow recovery of the diffraction intensity. The cooling time constant  $\tau$  was estimated to be  $123 \pm 12 \text{ ns}$  from the fitting curve. Guided by the extracted time scale, single-pulse imaging at that range was employed to capture the ultrafast eutectic process of the NWs (Fig. 4, bottom). Three rows of the single-shot images display the NW transient states after a single optical pulse (laser fluence of  $19.5 \text{ mJ/cm}^2$ ) at different delay times. The first, second and third column of the images was taken at the stages of before, at specific delays (20-100 ns), and after the process ended, respectively. It is noticed from the first-row images that besides a length shrinkage between the left (before) and middle (at 20 ns delay) image, a clear shape change of the top bead was observed (marked with a circle). The shape of the bead continued its change even after the incident laser pulse has been removed (right image). When the delay time was 80 ns (second row), similar behaviors, namely, the length shrinkage as well as the shape change, were also seen. However, the length and shape of the NW almost remained unchanged (third row) when observed at a delay time of 100 ns (middle) and at a state after the process ended (right). This observation indicates that the thermal energy induced by the laser heating pulse would not be sufficient to introduce a further obvious morphology change of the NW after a time of  $\sim 100 \text{ ns}$ .

As known, heating of composite materials by ultrafast laser pulses usually involves very large thermal gradients near the interface. With the incoming heating pulses, the top bead and the GaAs NW are “hot” but remain solid until regions of melt phase nucleate. Under a large thermal gradient it enables fast motion of the involved atoms of the melt phase near the interface. The melt phase starts to nucleate at the Au/GaAs interface and to expand into the materials. Nevertheless, thermal diffusion near the interface

limits the expansion of the melt region through cooling the photoexcited region. Therefore, after a short period of time, the temperature of the melt portion drops to the eutectic isotherm and the eutectic phases begin to nucleate and finally solidify to form the eutectic alloys.

For the scenario of a free-space diffusion process, we estimate the diffusion constant using  $l = \sqrt{2D\tau}$ , where  $l$  is the diffusion length,  $D$  is the diffusion coefficient and  $\tau$  is the time. From the single-shot images in Fig. 4, the NW length showed a  $\sim 30$  nm reduction at 20 ns (middle image in the first row) and continued a shrinkage of about 15 nm after the laser pulse (right image). The corresponding diffusion constant was estimated on an order of  $10^{-4}$  cm<sup>2</sup>/s, which is at least several orders of magnitude higher than the diffusivity of Au in GaAs and/or that of Ga in Au<sup>26-29</sup>. In comparison, the distance travelled by a ballistic gold or gallium atom with thermal velocity at the same temperature and time span would be on the order of microns, much larger than our observed NW length reduction. Therefore, the large reduction rate of the NW reported in this work suggests that the process cannot simply be diffusion-dominated processes, but rather indicates an important role due to the surface tension forces. Due to such surface-tension resultant forces, the reduction of 30 nm in NW length after a laser heating pulse could be fast, several orders of magnitude faster than the free-space diffusion or gravitational pull. The shape of the bead has maintained close to a sphere even though its size grows with number of laser heating pulses. Such spherical shape preservation is also an effect of surface tension, otherwise, the melt bead would drip down the GaAs NW similar to melt wax tearing down from a burning candle stick.

Furthermore, there was no obvious length change of the NW from 80 ns (middle image in the second row) to the end state (right image). Such observation provides an important clue about the time needed for eutectic reactions and solidification to complete. It indicates that the nucleation and growth of the melt eutectic phases were complete in  $\sim 80$  ns, and after that they began to solidify due to the cooling. The finding suggests that the eutectic reaction process of the NWs can be controlled/designed through tailoring

the fluence and number of laser pulses in the pulse sequence, providing the potential of eutectic bonding/welding to a desired/targeted location in micro/nanodevices. Additionally, the ability to fine tune the nanoparticle size and shape is important for plasmonics applications<sup>30-32</sup>.

Using 4D single-pulse imaging of multi-phase eutectic processes in nanostructured materials as an example, we clearly demonstrate the potential of this novel technique for exploring irreversible chemical/physical reaction dynamics at high spatial and temporal resolutions so that the underlying mechanisms in complex systems could be unraveled. By tuning the fluence and the sequence of laser heating pulses one could control the reaction dynamics at targeted positions and obtain the designed alloy phases. These powerful capabilities of 4D-EM provide in-situ manipulation and visualization of irreversible processes in space and time, and thus offers a valuable tool to investigate photochemical reactions as well as macromolecule dynamics in biological systems.

## Methods

**Preparation of Au/GaAs NWs.** The gold-catalyzed GaAs NWs were epitaxially grown on a GaAs (111)<sub>B</sub>-oriented substrate by metal-organic chemical vapor deposition. The catalysts used for the growth were gold nanoparticles. Initially, the GaAs substrate was treated with poly-L-lysine solution followed by a solution of colloidal Au nanoparticles ~100 nm in diameter. The major role of catalyst Au is to lower the nucleation energy of each grown layer at the seed/substrate interface, promoting the growth of NWs. Prior to growth, the substrate was annealed at 600 °C under AsH<sub>3</sub> ambient to remove surface contaminants. The substrate was then cooled to 550 °C, and the NW growth proceeded by injecting the precursors of trimethylgallium and AsH<sub>3</sub> to the growth chamber with ultra-high purity hydrogen as the carrier gas. Details of the growth procedures of GaAs NWs are available elsewhere<sup>33,34</sup>.

**Sample preparation for 4D imaging.** For EM sample preparation without any supporting films, the substrate containing free-standing GaAs NWs was cut into small pieces with dimensions of ~2×1×0.3 mm<sup>3</sup>. The small piece was glued on a common copper O-ring. Then the copper O-ring with the sample was directly mounted on the EM holder for investigation (see Fig. 1c). This method of sample preparation excludes any disturbance from the supporting films normally present in EM grids.

**Spatiotemporal visualization of eutectic dynamics.** The morphology of GaAs NWs was investigated using an FEI scanning electron microscope. The studies of the eutectic dynamics and control of Au/GaAs NWs were conducted by 4D-EM (Fig. 1a). The 4D-EM is equipped with laser systems, which can operate in either stroboscopic (for reversible processes) or single-pulse mode (for irreversible dynamics). Both modes were used in this work. Picosecond (ps) green laser pulses at 532 nm (16 ps pulse duration) were used to heat the sample and to initiate the reactions, whereas nanosecond (ns) ultraviolet laser pulses at

266 nm (10 ns pulse duration) were directed to the photocathode to generate electron pulses. The photoelectrons in each pulse for probing were then accelerated to 120 keV, corresponding to a de Broglie wavelength of 3.3 pm. The timing between the pump pulse and the probe pulse was controlled by changing the delay time between the two through a digital delay generator.

## **Acknowledgements**

We acknowledge the financial support from the Air Force Office of Scientific Research (Grant No. FA9550-11-1-0055S) in the Gordon and Betty Moore Foundation for Physical Biology Center for Ultrafast Science and Technology at California Institute of Technology. The Australian authors thank the Australian Research Council for the financial support and the Australian National Fabrication Facility for access to the epitaxial facilities used in this work.

## **Author contributions**

B.C. and A.H.Z. conceived the experiment, B.C. and X.W.F. designed and conducted the experiment, J.T. performed theoretical modeling and data analysis, M.L., H.H.T. and C.J. grew the samples, all authors analyzed the data and wrote the paper.

**Table 1. Latent heat and specific heat for two phases.**

<b>Phase</b>	<b>Temperature (K) (23)</b>	<b>Latent heat (kJ/mol)</b>	<b>Specific heat (J/mol.K)</b>
Au <sub>7</sub> Ga <sub>2</sub>	555	8	62
AuGa	620	21	41

## Figure captions

**Figure 1. 4D electron microscopy for imaging phase reactions in a free-standing NW.** (a) Picosecond green optical pulse enables the eutectic reaction of Au/GaAs NWs to be probed by a delayed electron pulse (generated by a nanosecond ultraviolet laser pulse) at a given time delay. (b) Scheme of free-standing NWs on substrate integrated in 4D-EM. The laser heating pulse is incident upon the NW at a nearly vertical angle while a series of eutectic events are captured by single-pulse methodology. (c) Projections of the NWs. The NWs were intentionally grown far apart from each other to exclude mutual perturbation during the measurement.

**Figure 2. Images, diffractions and tomography micrographs of the Au/GaAs NWs.** Top row: Stroboscopic image of the NW and its diffraction pattern (marked circle in the image). The diffraction pattern indicates a hexagonal WZ structure of GaAs. Middle row: Image and diffraction pattern of the NW tip region. Additional diffraction spots appeared besides the same ones as that in the top row. These extra spots are from the cubic ZB segments, which can be seen from an enlarged image in the inset of the left image. Scale bar, 50 nm. Bottom row: Images of the NW at different tilting angles ranging from  $-10^\circ$  to  $50^\circ$ . At all angles the NW is straight, suggesting that neither inclination nor breakage of the NW occurred during the laser pulse excitation.

**Figure 3. Single-shot imaging of transient changes of the NW, and the calculated temperatures.** Top: Single-shot imaging of the NW length reduction due to eutectic reactions. The NW shrank along its axial direction while its lateral width had no obvious change. More than 50% length reduction was observed after a total of 46 laser shots. The rulers (white lines) indicate the length. Bottom left: Volume change of the NW. The volume reduction of GaAs NW and the volume increase of top bead was almost the same, indicating no obvious change of the total volume. Bottom right: Calculated temperatures at different laser

fluences. The temperature of Au or GaAs bead was estimated by assuming 100% of the component while the effective temperature of the bead was calculated by considering the Au:GaAs ratio in the bead. The dotted line represents the lowest temperature to trigger the reaction. Because of the large latent heat of GaAs, the GaAs NW has not melted though the temperatures (without taking account of the latent heat) are higher than its melting point (dashed line) at high fluences. The solid red line indicates the actual temperature of the GaAs NW when its latent heat is considered.

**Figure 4. Time-resolved ultrafast dynamics of the NW.** Top: Normalized diffraction intensity vs. delay time, indicating a cooling dynamics with the time constant of  $123 \pm 12$  ns. The fitting is shown in the red line. Bottom: single-shot images of the NW at a specific delay time. The images in the left, middle and right columns correspond to the states of the NW before, at specific delays, and after the process ended (the incident laser pulse has been removed), respectively. Three rows of images are associated with the NW states at the delay time of 20, 80 and 100 ns, respectively. Besides the length shrinkage, the transient shape changes of the top bead (marked with a circle) at different delays were also captured. The white rulers indicate the length.

## References

1. Nadella, R., Eskin, D. G., Du, Q. & Katgerman, L. Macrosegregation in direct-chill casting of aluminium alloys. *Prog. Mater. Sci* **53**, 421-480 (2008).
2. Woodall, J. M. III-V compounds and alloys: An update. *Science* **208**, 908-915 (1980).
3. del Alamo, J. A. Nanometre-scale electronics with III-V compound semiconductors. *Nature* **479**, 317-323 (2011).
4. Wolffenbuttel, R. F. & Wise, K. D. Low-temperature silicon wafer-to-wafer bonding using gold at eutectic temperature. *Sens. Actuators A* **43**, 223-229 (1994).
5. Kim, B. J., Tersoff, J., Kodambaka, S., Reuter, M. C., Stach, E. A. & Ross, F. M. Kinetics of individual nucleation events observed in nanoscale vapor-liquid-solid growth. *Science* **322**, 1070-1073 (2008).
6. Schüllli, T. U., Daudin, R., Renaud, G., Vaysset, A., Geaymond, O. & Pasturel, A. Substrate-enhanced supercooling in AuSi eutectic droplets. *Nature* **464**, 1174-1177 (2010).
7. Shpyrko, O. G., Streitel, R., Balagurusamy, V. S. K., Grigoriev, A. Y., Deutsch, M., Ocko, B. M., Meron, M., Lin, B. & Pershan, P. S. Surface crystallization in a liquid AuSi alloy. *Science* **313**, 77-80 (2006).
8. LLorca, J. & Orera, V. M. Directionally solidified eutectic ceramic oxides. *Prog. Mater. Sci.* **51**, 711-809 (2006).
9. Rosa, C. D., Park, C., Thomas, E. L. & Lotz, B. Microdomain patterns from directional eutectic solidification and epitaxy. *Nature* **405**, 433-437 (2000).

10. Kodambaka, S., Tersoff, J., Reuter, M. C. & Ross, F. M. Germanium nanowires growth below the eutectic temperature. *Science* **316**, 729-732 (2007).
11. Holmberg, V. C., Panthani, M. G. & Korgel, B. A. Phase transitions, melting dynamics, and solid-state diffusion in a nano test tube. *Science* **326**, 405-407 (2009).
12. Shahani, A. J., Xiao, X. H. & Voorhees, P. W. The mechanism of eutectic growth in highly anisotropic materials. *Nat. Commun.* **7**, 12953 (2016).
13. Barwick, B., Flannigan, D. J. & Zewail, A. H. Photo-induced near-field electron microscopy. *Nature* **462**, 902-906 (2009).
14. Zewail, A. H. Four-dimensional electron microscopy. *Science* **328**, 187-193 (2010).
15. van der Veen, M. R., Kwon, O. H., Tissot, A., Hauser, A. & Zewail, A. H. Single-nanoparticle phase transitions visualized by four-dimensional electron microscopy. *Nat. Chem.* **5**, 395-402 (2013).
16. Baskin, J. S., Liu, H. H. & Zewail, A. H. 4D multiple-cathode ultrafast electron microscopy. *Proc. Natl. Acad. Sci. USA* **111**, 10479-10484 (2014).
17. Lorenz, U. J. & Zewail, A. H. Observing liquid flow in nanotubes by 4D electron microscopy. *Science* **344**, 1496-1500 (2014).
18. Lobastov, V. A., Srinivasan, R. & Zewail, A. H. Four-dimensional ultrafast electron microscopy. *Proc. Natl. Acad. Sci. USA* **102**, 7069-7073 (2005).
19. Barwick, B., Park, H. S., Kwon, O. H., Baskin, J. S. & Zewail, A. H. 4D imaging of transient structures and morphologies in ultrafast electron microscopy. *Science* **322**, 1227-1231 (2008).

20. Park, S. T., Flannigan, D. J. & Zewail, A. H. Irreversible chemical reactions visualized in space and time with 4D electron microscopy. *J. Am. Chem. Soc.* **133**, 1730-1733 (2011).
21. Chen, B., Wang, J., Gao, Q., Chen, Y. J., Liao, X. Z., Lu, C. S., Tan, H. H., Mai, Y. W., Zou, J., Ringer, S. P., Gao, H. & Jagadish, C. Strengthening brittle semiconductor nanowires through stacking faults: Insights from in situ mechanical testing. *Nano Lett.* **13**, 4369-4373 (2013).
22. Joyce, H. J., Gao, Q., Tan, H. H., Jagadish, C., Kim, Y., Zou, J., Smith, L. M., Jackson, H. E., Yarrison-Rice, J. M., Parkinson, P. & Johnston, M. B. III-V semiconductor nanowires for optoelectronic device applications. *Prog. Quant. Electron.* **35**, 23-75 (2011).
23. Wang, J., Liu, Y. J., Liu, L. B., Zhou, H. Y. & Jin, Z. P. Thermodynamic assessment of the Au-Ga binary system. *CALPHAD* **35**, 242-248 (2011).
24. Blakemore, J. S. Semiconducting and other major properties of gallium arsenide. *J. Appl. Phys.* **53**, R123-181 (1982).
25. Kuanr, A. V., Bansal, S. K. & Srivastava, G. P. Laser induced damage in GaAs at 1.06  $\mu\text{m}$  wavelength: surface effects. *Opt. Laser Technol.* **28**, 25-34 (1996).
26. Patuwathavithane, C. S., Williams, J. R., Tin, C. C., Barnes, P. A. & Bozack, M. J. An RBS analysis of the low temperature mass transport of Au in GaAs. *Nucl. Instrum. Methods Phys. Res.* **B56/57**, 753-756 (1991).
27. Fisher, D. J. Diffusion in GaAs and Other III-V Semiconductors: 10 Years of Research (Trans Tech Publications, Switzerland, 1998).
28. Gupta, R. P., Khokle, W. S., Wuerfl, J. & Hartnagel, H. L. Diffusion of gallium in thin gold films on GaAs. *Thin Solid Films* **151**, L121-L125 (1987).

29. Persson, A. I., Larsson, M. W., Stenström, S., Ohlsson, B. J., Samuelson, L. & Wallenberg, L. R. Solid-phase diffusion mechanism for GaAs nanowire growth. *Nat. Mater.* **3**, 677-681 (2004).
30. Jin, R., Cao, Y. W., Mirkin, C. A., Kelly, K. L., Schatz, G. C. & Zheng, J. G. Photoinduced conversion of silver nanospheres to nanoprisms. *Science* **294**, 1901-1903 (2001).
31. Jain, P. K., Huang, X., El-Sayed, I. H. & El-Sayed, M. A. Noble metals on the nanoscale: optical and photothermal properties and some applications in imaging, sensing, biology, and medicine. *Acc. Chem. Res.* **41**, 1578-1586 (2008).
32. Byers, C. P., Zhang, H., Swearer, D. F., Yorulmaz, M., Hoener, B. S., Huang, D., Hoggard, A., Chang, W. S., Mulvaney, P., Ringe, E., Halas, N. J., Nordlander, P., Link, S. & Landes, C. F. From tunable core-shell nanoparticles to plasmonic drawbridges: Active control of nanoparticle optical properties. *Sci. Adv.* **1**, e1500988 (2015).
33. Joyce, H. J., Gao, Q., Tan, H. H., Jagadish, C., Kim, Y., Zhang, X., Guo, Y. & Zou, J. Twin-free uniform epitaxial GaAs nanowires grown by a two-temperature process. *Nano Lett.* **7**, 921-926 (2007).
34. Joyce, H. J., Wong-Leung, J., Gao, Q., Tan, H. H. & Jagadish, C. Phase perfection in zinc blende and wurtzite III-V nanowires using basic growth parameters. *Nano Lett.* **10**, 908-915 (2010).

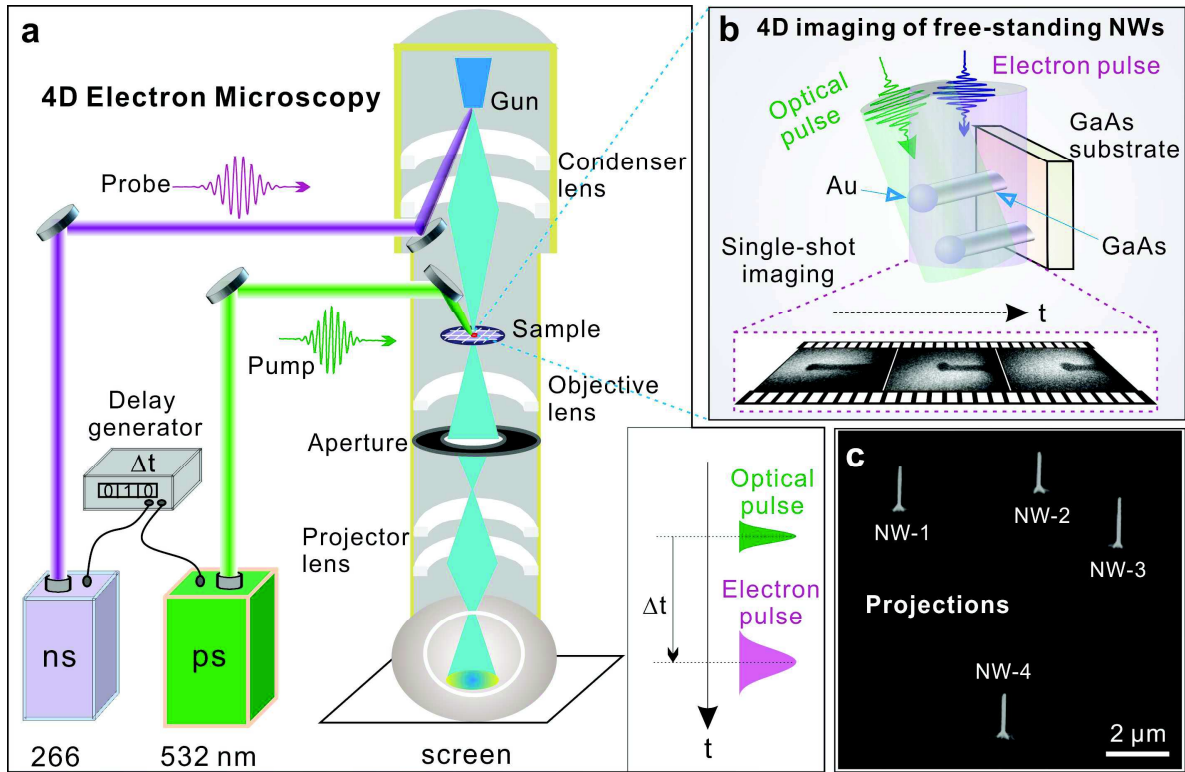


**Figure 1**

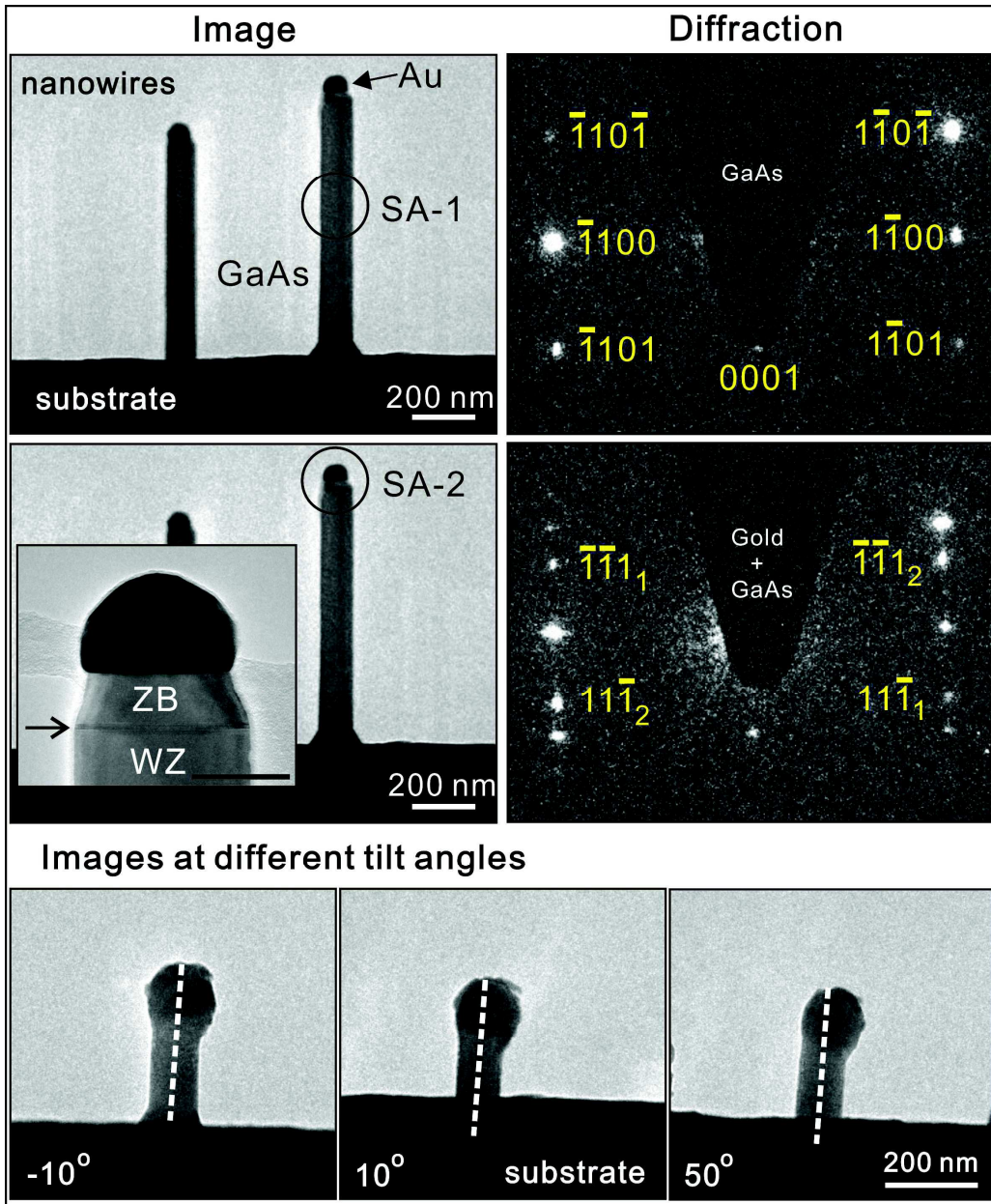


**Figure 2**

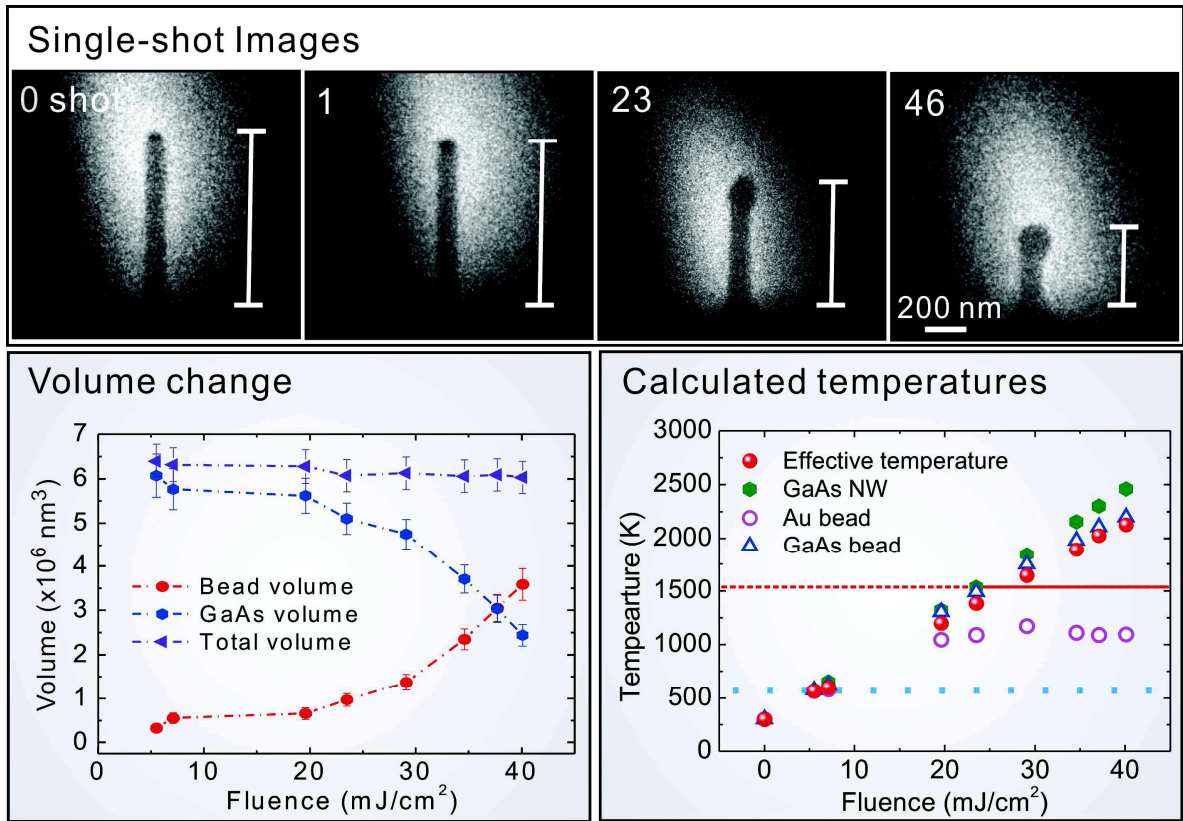


**Figure 3**

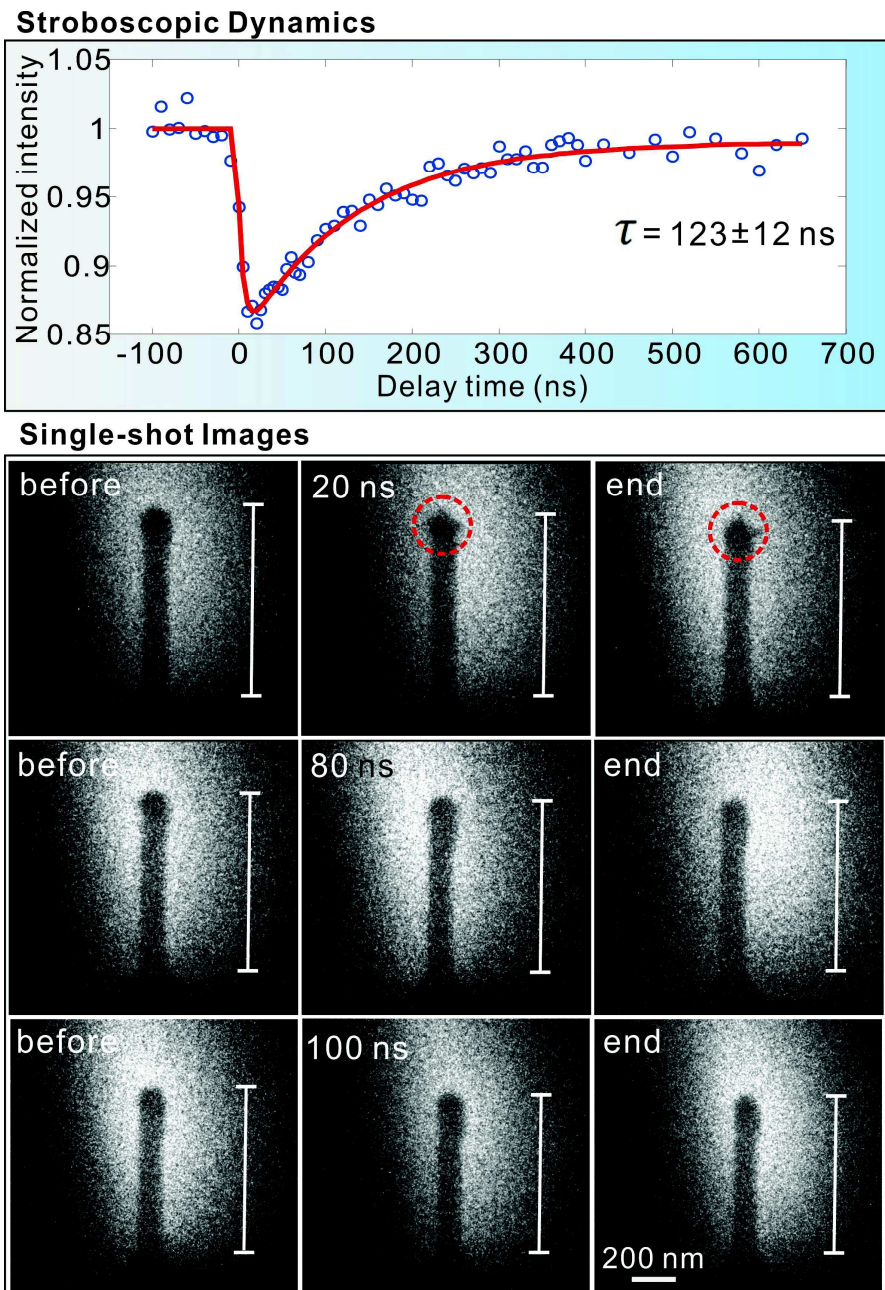


**Figure 4**

## Supplementary Information for

# Eutectic dynamics and control of gold-encapped gallium arsenide nanowires imaged by 4D electron microscopy

Bin Chen,<sup>1,\*</sup> Xuewen Fu,<sup>1</sup> Jau Tang,<sup>1,\*</sup> Mykhaylo Lysevych,<sup>2</sup> Hark Hoe Tan,<sup>3</sup> Chennupati Jagadish,<sup>3</sup>  
Ahmed H. Zewail<sup>1,†</sup>

<sup>1</sup>Physical Biology Center for Ultrafast Science and Technology, Arthur Amos Noyes Laboratory of Chemical Physics, California Institute of Technology, Pasadena, CA 91125, USA

<sup>2</sup>Australian National Fabrication Facility, Research School of Physics and Engineering, The Australian National University, Canberra, ACT 2601, Australia

<sup>3</sup>Department of Electronic Materials Engineering, Research School of Physics and Engineering, The Australian National University, Canberra, ACT 2601, Australia

\*Corresponding author. Email: [bchen5@caltech.edu](mailto:bchen5@caltech.edu), [jautang@caltech.edu](mailto:jautang@caltech.edu)

†Deceased

The PDF file includes:

Supplementary Notes

Supplementary Figures 1 to 5

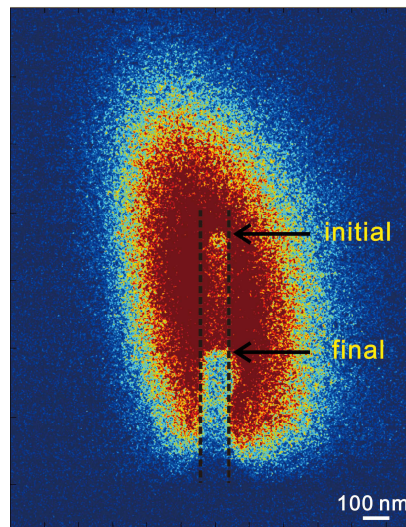
Supplementary Tables 1 to 2

Supplementary References

## Supplementary Notes

### Width change of the NW

Supplementary Figure 1 shows a micrograph of the superposition with two EM images. Those two images correspond to the initial and final state of the NW, respectively. Because GaAs was incorporated into the top Au bead that enabled the eutectic reactions, the final top bead became bigger than the initial one. However, it is noteworthy that the width of the NW body shows no obvious change.



**Supplementary Figure 1.** Superposition of two EM images of a NW, before *vs.* after laser excitation. The dashed lines indicate the left and right edges of the NW.

### Volume change of the NW

The volume change of the NW was estimated according to the schematics shown in Supplementary Fig. 2. GaAs has a hexagonal shape in cross-sectional geometry<sup>1</sup> while the initial Au bead shows a segment shape of a sphere. The initial volume  $V_0$  of the Au/GaAs is,

$$V_0 = S \times l + 4/3 \pi R^3 - \pi(R - m)^2 \times \left(R - \frac{R-m}{3}\right) \quad (1)$$

where  $l$  and  $S$  are the length and cross-sectional area of GaAs,  $R$  is the initial radius of the Au bead and  $m$  is the height from the center point to the bottom of the sphere segment. Based on the hexagonal geometry,  $S$  equals to  $\frac{3\sqrt{3}}{2}d^2$ , where  $d$  is the half width of the GaAs NW.

The volume reduction of the GaAs NW as a result of the length shrinkage  $\Delta l$  becomes,

$$\Delta V_1 = \Delta l \times S \quad (2)$$

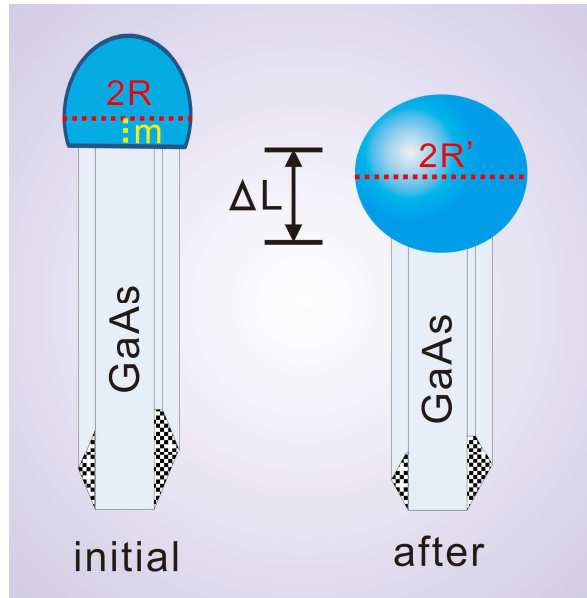
The volume increase of the top bead with a final radius of  $R'$  is given by,

$$\Delta V_2 = 4/3 \pi R'^3 - [4/3 \pi R^3 - \pi(R - m)^2 \times (R - \frac{R-m}{3})] \quad (3)$$

Therefore, the total volume change of the Au/GaAs is written as,

$$\Delta V = \Delta V_1 + \Delta V_2 \quad (4)$$

Substituting the parameters  $l$ ,  $\Delta l$ ,  $R$ ,  $R'$ ,  $m$ , and  $d$  measured from the EM images into equations (1)-(4), the volume changes of the bead and the NW are plotted in Fig. 3 of the main text.



**Supplementary Figure 2.** Schematic diagram of the NW and the bead used for estimation of the volume changes. GaAs has a hexagonal cross-section with an area of  $S$ . The length change  $\Delta l$  of GaAs

was measured by the difference between the initial length and the one after a laser shot. The initial Au bead shows a segment of a sphere with a diameter and height of  $2R$  and  $(R + m)$ , respectively. The top bead after laser excitation is assumed to be a sphere with a diameter of  $2R'$ .

### Newly formed alloy phases after laser excitation

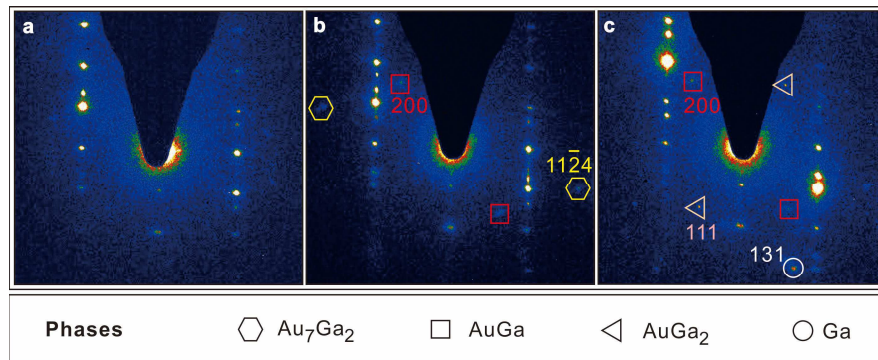
Supplementary Figure 3 show the diffraction patterns of the top part of the NW before and after the laser excitation. These images were taken under the off-axis conditions so that the diffraction intensities from the newly formed phases were enhanced. In the initial state (Supplementary Fig. 3a), the diffraction spots were from GaAs, similar as that shown in Fig. 2 of the main text. After the first three laser pulses, however, additional diffraction spots were seen (Supplementary Fig. 3b). Those spots were from  $\text{Au}_7\text{Ga}_2$   $\{11\bar{2}4\}$  and  $\text{AuGa}$   $\{200\}$ , respectively. The lattice constants used for the identification of those phases are listed in Supplementary Table 1. In the final state (Supplementary Fig. 3c), namely, as more GaAs component was incorporated into the top bead, new phases from  $\text{AuGa}_2$   $\{111\}$  and  $\text{Ga}$   $\{131\}$  were detected besides the  $\text{AuGa}$  phase. It is not favorable for the alloy formation between As and Au components, and the As species may vaporize or be removed from the interface during the laser heating<sup>4,5</sup>.

**Supplementary Table 1. Lattice constants of the newly formed phases.**

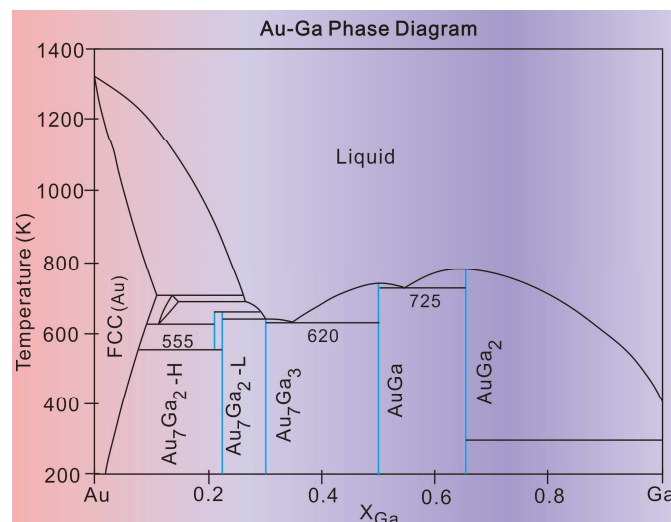
Phases	Structures	a (Å)	b (Å)	c (Å)	Reference
$\text{Au}_7\text{Ga}_2$	Hexagonal	7.725	/	8.741	[2, 3]
$\text{AuGa}$	Orthorhombic	6.397	6.262	3.463	
$\text{AuGa}_2$	Cubic	6.076	/	/	
$\text{Ga}$	Orthorhombic	4.519	7.657	4.526	

### Phase diagram of Au-Ga binary system

From the diffraction analysis the newly formed phases in the top bead are identified as Au-Ga alloys. Supplementary Figure 4 presents the Au-Ga binary phase diagram<sup>3,6</sup>. The melting points of



**Supplementary Figure 3.** Diffraction patterns from the top part of the NW. (a) Initial state without any laser pulse. (b) After the first three laser pulses. New phases, Au<sub>7</sub>Ga<sub>2</sub> and AuGa, were detected. (c) Final state after 46 laser pulses. AuGa, AuGa<sub>2</sub> and Ga phases were present. The hexagonal, rectangular, triangular and circular symbols represent the phases of Au<sub>7</sub>Ga<sub>2</sub>, AuGa, AuGa<sub>2</sub> and Ga, respectively.



**Supplementary Figure 4.** Au-Ga binary phase diagram redrawn from refs. 3 and 6. The horizontal axis is the atomic fraction of Ga component.

Au and GaAs are 1337 and 1511 K, respectively. However, the temperature needed for the eutectic reaction can be much lower than the melting point of any pure component. For example, to obtain the phases of Au<sub>7</sub>Ga<sub>2</sub> and AuGa, the temperatures are ~555 and 620 K, respectively. On the other hand, the temperature needed for the eutectic reaction of liquid  $\rightarrow$  AuGa + AuGa<sub>2</sub> is about 725 K.

### Modeling of laser heating of gold and GaAs

Laser heating of a GaAs NW with a Au tip and the induced eutectic phase reaction can be modeled using the following theoretical approach. First, we consider laser heating of Au nanoparticle alone using the conventional two-temperature model (TTM) which deals with temporal and spatial temperature changes for both electron and phonon subsystems. Then, we treat laser heating of a GaAs NW using a three-temperature model (3TM) to deal with the temporal and spatial evolution of charged carrier density, carrier temperature, optical phonon temperature and acoustic phonon temperature. Because the optical reflectivity could be influenced by the nanoparticle size (Supplementary Fig. 5), in our simulations for a given bead size we have incorporated empirical size-dependent reflectivity reported in literature<sup>7-13</sup>. To calculate the lattice temperature for the bead with a mixture of Au and alloy, the following approach was used. We first calculated the lattice temperature for a bead of Au (assuming 100% Au) and also a bead of GaAs (100% GaAs), and then we estimated the effective lattice temperature based on their composition percentage within the bead. This approximation is a necessary step in the simulation because the actual optical and thermal parameters for TTM and 3TM modeling of a composite nanoparticle have not been known in literature.

According to the TTM with a laser beam along the z-axis, the evolution of the electron temperature  $T_e(z, t)$  and the lattice temperature  $T_L(z, t)$  follows<sup>14-16</sup>,

$$C_e \frac{\partial}{\partial t} T_e(z, t) = \frac{\partial}{\partial z} \left( k_e \frac{\partial}{\partial z} T_e(z, t) \right) - g[T_L(z, t) - T_e(z, t)] + S(z, t)$$

$$C_L \frac{\partial}{\partial t} T_L(z, t) = -g[T_e(z, t) - T_L(z, t)] \quad (5)$$

where  $C_L$  is the specific heat for phonons, and  $S(z, t)$  is the incident laser pulse profile. At a low laser excitation fluence, one usually assumes that the electron/phonon coupling  $g$  is a constant, the specific heat  $C_e$  for electrons has linear dependence on electron temperature, and the electronic thermal conductivity  $k_e$  is approximated by  $K_e T_e / T_L$ . Such approximations have shown to be inaccurate for electron temperature beyond 3000 K. Here we use the following improved formulae for their temperature dependence,

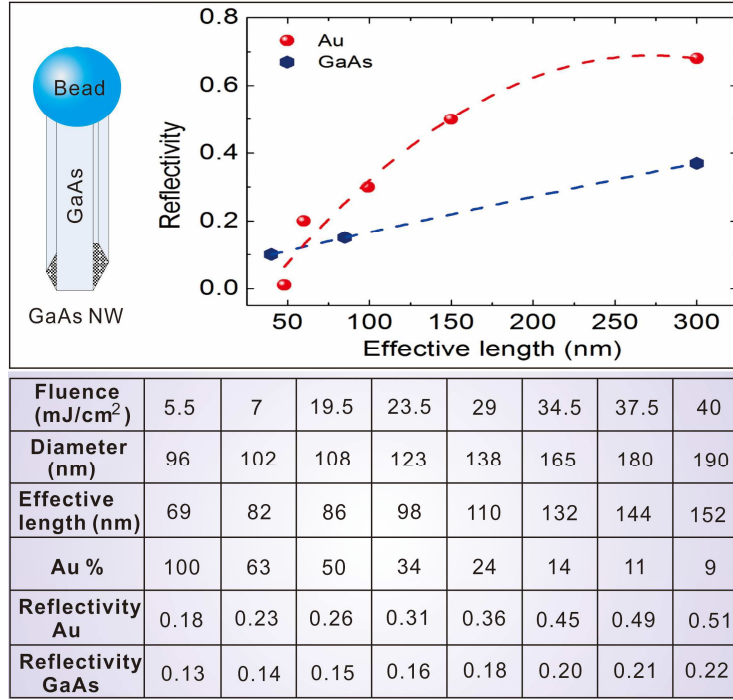
$$k_e = \frac{4.26 \times 10^{13} T_e}{1.20 \times 10^7 T_e^2 + 1.23 \times 10^{11} T_L} \quad (6)$$

and Padé approximation for the electron/phonon  $g$  and  $C_e$ , respectively,

$$g = 1.0 \times 10^{17} \frac{\sum_{n=0}^4 A_1(n) (T_e/10^4)^n}{1 + \sum_{n=1}^4 A_2(n) (T_e/10^4)^n}$$

$$C_e = 1.0 \times 10^{17} \frac{\sum_{n=0}^3 B_1(n) (T_e/10^4)^n}{1 + \sum_{n=1}^3 B_2(n) (T_e/10^4)^n} \quad (7)$$

where  $A_1(0) = 0.257$ ,  $A_1(1) = -0.549$ ,  $A_1(2) = 0.553$ ,  $A_1(3) = -0.650$ , and  $A_1(4) = 6.269$ ;  $A_2(1) = -2.544$ ,  $A_2(2) = 4.566$ ,  $A_2(3) = -1.479$ , and  $A_2(4) = 2.541$ ;  $B_1(0) = -0.043$ ,  $B_1(1) = 8.451$ ,  $B_1(2) = -28.797$ , and  $B_1(3) = 68.387$ ;  $B_2(1) = -1.645$ ,  $B_2(2) = 2.539$ , and  $B_2(3) = 0.702$ . All other relevant parameters for Au and GaAs are listed in Supplementary Fig. 5.



**Supplementary Figure 5.** Top: The size-dependent reflectivity of Au and GaAs<sup>7-13</sup>. Bottom: The reflectivity of Au and GaAs adjusted according to their actual size observed in the experiment. To simplify the theoretical modeling, a cube-shaped top bead for the corresponding spherical volume was assumed. The diameter of the bead was converted to the effective length of the cube. The gold percentage was estimated by the ratio of initial gold volume to the final bead volume.

For laser heating of a GaAs NW with an incident intensity profile  $I(z, t)$ , we employed three-temperature model (3TM) that describes time evolution of four subsystems, namely, the charge carrier density  $N_c(z, t)$ , and three subsystem temperatures such as carrier temperature, optical and acoustic phonon temperatures. Defining the internal energy for the charge carriers  $U_c(z, t)$ , and the internal energy for the longitudinal optical (LO) phonons  $U_o(z, t)$  and the longitudinal acoustic (LA) phonons  $U_A(z, t)$ , one has<sup>17-19</sup>,

$$\frac{\partial}{\partial t} N_C(z, t) = \frac{\alpha_1 I(z, t)}{\hbar\omega} - \gamma_A N_C^3(z, t)$$

$$\begin{aligned} \frac{\partial}{\partial t} U_C(z, t) = \frac{\partial}{\partial z} \left[ k_C \frac{\partial}{\partial z} T_C(z, t) \right] + \alpha_1 I(z, t) - \frac{3k_B N_C(z, t)}{2} \left[ \frac{T_C(z, t) - T_O(z, t)}{\tau_{C-O}} \right] \\ - \frac{3k_B N_C(z, t)}{2} \left[ \frac{T_C(z, t) - T_A(z, t)}{\tau_{C-A}} \right] \end{aligned}$$

$$\frac{\partial}{\partial t} U_O(z, t) = \frac{3k_B N_C(z, t)}{2} \left[ \frac{T_C(z, t) - T_O(z, t)}{\tau_{C-O}} \right] - C_O \left[ \frac{T_O(z, t) - T_A(z, t)}{\tau_{O-A}} \right]$$

$$\frac{\partial}{\partial t} U_A(z, t) = \frac{\partial}{\partial z} \left[ k_A \frac{\partial}{\partial z} T_A(z, t) \right] + \frac{3k_B N_C(z, t)}{2} \left[ \frac{T_C(z, t) - T_A(z, t)}{\tau_{C-A}} \right] + C_O \left[ \frac{T_O(z, t) - T_A(z, t)}{\tau_{O-A}} \right] - h(T_A(z, t) - T_B) \quad (8)$$

where the internal energies for the carriers, the LO phonons and the acoustic phonons are given by,

$$U_C = N_C E_g + C_C T_C$$

$$U_O = C_O T_O$$

$$U_A = C_A T_A \quad (9)$$

The relevant physical parameters for the 3TM, their nomenclature and their dependence on temperature and carrier density are given in Supplementary Table 2.

**Supplementary Table 2. The parameters of GaAs used in the three-temperature model.**

Physical Property	Value	Reference
Heat capacity of carriers $C_C$ (J/m <sup>3</sup> K)	$C_C = 3N_C k_B$	[19]

Heat capacity of LO phonons $C_{LO}$ (J/m <sup>3</sup> K)	$C_{LO} = 3.06 \times 10^5 - 2.4 \times 10^4 (\theta_{LO}/T_O)^{1.94}$ where $\theta_{LO} = 344$ K	[18, 20]
Heat capacity of acoustic phonons $C_A$ (J/m <sup>3</sup> K)	$C_A = 9.17 \times 10^5 - 4.40 \times 10^4 (\theta_D/T_A)^{1.948}$ where Debye temperature $\theta_D = 344$ K	[19, 20]
Thermal conductivity of carriers $k_C$ (W/m K)	$k_C = 2.5 \times N_C k_B^2 \tau_m T_C / m^*$ where $m^* = 0.066 m_e$ , $\tau_m = 0.3$ ps	[18, 21]
Thermal conductivity of acoustic phonons $k_A$ (W/m K)	$k_A = 4.0 \times 10^4 / T_A^{1.2}$	[18, 22]
Energy relaxation time between carriers and LO phonons $\tau_{C-O}$	$\tau_{C-O} = 0.1 \times 10^{-12}$ (s)	[23]
Energy relaxation time between carriers and acoustic phonons $\tau_{C-A}$	$\tau_{C-A} = 0.5 \times 10^{-12} [1 + (N_C/N_O)^2]$ where $N_O = 2 \times 10^{27}$ (1/m <sup>3</sup> )	[18, 19]
Energy relaxation time between LO and acoustic phonons $\tau_{O-A}$	$\tau_{O-A} = 8 \times 10^{-12}$ (s)	[18, 24]
Absorption coefficient $\alpha_1$ (1/m)	$\alpha_1 = 3.48 \times 10^6 \exp[1.71 \times (x - 1.83)]$ $x = \hbar\omega + E_g(300) - E_g(T_p)$ (eV)	[22]
Auger coefficient $\gamma_A$ (m <sup>6</sup> /s)	$\gamma_A = 1.0 \times 10^{-43}$	[25, 26]
Band gap $E_g$ (eV)	$E_g(T_p) = 1.575 - 0.15(T_p/300)$	[22, 27]

Linear thermal expansion coefficient $\beta$	$\beta = 5.7 \times 10^{-6} \text{ (K}^{-1}\text{)}$	[28]
Ga-As interatomic distance $\ell$	$\ell = 4.00 \text{ \AA}$	[29]
Sound velocity $v_s$	$v_s = 4730 \text{ m/s}$	[30]

### Quantitative analysis for the eutectic growth of alloy phases

#### 1. Laser fluence at $5.5 \text{ mJ/cm}^2$

From our studies we could extract some important thermal properties which have not been tabulated in the literature, such as latent heat and heat capacity for the alloy phases during the eutectic growth upon laser heating of the Au/GaAs NWs. To facilitate quantitative analysis of the experimental data including the length reduction of the GaAs NW and the size increment of the bead after each laser pulse, we have employed TTM for gold and 3TM for GaAs to estimate the heat energy absorbed by the NW and the bead upon each laser pulse excitation at a given fluence. According to our simulation, after the 1<sup>st</sup> laser pulse with a fluence of  $5.5 \text{ mJ/cm}^2$ , the calculated lattice temperatures for the Au bead (566 K) and the GaAs NW (574 K) are above the temperature of  $\sim 555 \text{ K}$  needed for the  $\text{Au}_7\text{Ga}_2$  phase formation. Therefore, at this fluence those Ga atoms from the disappearing NW volume, corresponding to a length reduction of 25 nm and a hexagonal cross section with a side length of 54 nm, are expected to undergo the reaction with the encapped Au atoms at the tip to form  $\text{Au}_7\text{Ga}_2$  alloy. The excessive heat energy above the temperature (555 K) from the tip and the NW allows us to estimate the latent heat for the alloy formation. Based on the parameters including the molar volumes (Au:  $1.0 \times 10^{-5} \text{ m}^3/\text{mol}$ , GaAs:  $2.7 \times 10^{-5} \text{ m}^3/\text{mol}$ ), the heat capacities (Au:  $2.49 \times 10^6 \text{ J/m}^3 \cdot \text{K}$ , GaAs:  $1.76 \times 10^6 \text{ J/m}^3 \cdot \text{K}$ )<sup>29,31</sup>, the densities (Au:  $1.93 \times 10^4 \text{ kg/m}^3$ , GaAs:  $5.32 \times 10^3 \text{ kg/m}^3$ ,  $\text{Au}_7\text{Ga}_2$ :  $1.67 \times 10^4 \text{ kg/m}^3$ )<sup>32</sup> and the molar ratio of 7:2 for  $\text{Au}_7\text{Ga}_2$ , we obtained the latent heat of 8 kJ/mol for the  $\text{Au}_7\text{Ga}_2$  alloy.

After the 2<sup>nd</sup> laser pulse at the same fluence but with a larger bead of a mixture of gold and alloy, we observed an additional 3 nm length reduction for the NW. According to the 3TM modeling, we obtained a lattice temperature of 574 K for the GaAs NW. For the top bead, the calculated lattice temperatures were 510 and 567 K when 100% gold and 100% GaAs were assumed in the bead, respectively. Using these temperature values and the molar percentage in the bead, we obtained the absorbed heat from the additional bead volume and from the NW with the values of  $1.5 \times 10^{-14}$  J and  $1.1 \times 10^{-14}$  J, respectively. We defined the net heat as the energy needed to raise the bead for the volume reduction in the NW (3 nm times the hexagonal cross-section area of the NW) from room temperature to 555 K. This net heat was calculated from the overall absorbed heat of the bead and the NW subtracting two parts: first, the heat for raising the temperature to 555 K for the gold molar volume (a 7/2 ratio times the Ga molar volume from the reduction of the NW volume); second, the latent heat of the corresponding Ga molar volume from the reduction of the NW volume. Knowing the density of Au<sub>7</sub>Ga<sub>2</sub>, the specific heat of the Au<sub>7</sub>Ga<sub>2</sub> alloy was estimated to be 62 J/mol.K.

After the 3<sup>rd</sup> laser pulse at the same fluence, we observed 1 nm length reduction for the NW. Following the similar approach, a lattice temperature of 574 K for the GaAs NW was obtained. The calculated lattice temperatures of the top bead were 507 and 567 K when 100% gold and 100% GaAs were assumed, respectively. Using the similar procedures outlined above, we extracted the specific heat for the Au<sub>7</sub>Ga<sub>2</sub> alloy to be 60 J/mol.K, which is close to the value obtained from the 2<sup>nd</sup> pulse laser heating.

## 2. Laser fluence at 7 mJ/cm<sup>2</sup>

After three laser pulses at 5.5 mJ/cm<sup>2</sup>, the NW length was shortened by 25, 3 and 1 nm sequentially, and the bead stopped to grow. To continue the reaction dynamics, the laser fluence was

increased to  $7 \text{ mJ/cm}^2$ . Using the similar simulation approach and the experimental observation of a further 10 nm length reduction of the NW, we obtained the lattice temperatures of 658 K for the GaAs NW, 587 K for a 100% gold bead and 649 K for a 100% GaAs bead, and the overall effective temperature was above the temperature of  $\sim 620 \text{ K}$  needed for AuGa phase. The absorbed energies from the volume reduction of the NW and from the bead with a mixed composition are  $4.8 \times 10^{-14} \text{ J}$  and  $5.3 \times 10^{-14} \text{ J}$ , respectively. To calculate the latent heat of AuGa, one needs to deduct the latent heat of  $\text{Au}_7\text{Ga}_2$  phase and also the energy needed to raise the alloy from room temperature to 620 K for AuGa. These two parts of heat to be subtracted from the overall absorbed laser heat is  $2.3 \times 10^{-14} \text{ J}$ . Using the density of  $1.28 \times 10^4 \text{ kg/m}^3$  for  $\text{AuGa}^{32}$ , its latent heat was estimated to be about 21 kJ/mol.

After the 2<sup>nd</sup> laser pulse at the same fluence, a 3 nm length reduction of the NW was further observed. Based on the 3TM modeling, the lattice temperature of the GaAs NW is found to be 658 K. For the top bead, the calculated lattice temperatures are 571 K for a 100% Au bead and 645 K for a 100% GaAs bead, respectively. Using these temperature values and the molar percentage in the bead, we estimated the absorbed heat from the additional bead volume and from the NW to be  $6.6 \times 10^{-15} \text{ J}$  and  $4.8 \times 10^{-15} \text{ J}$ , respectively. According to the similar procedures mentioned above, we obtained the net heat of  $4.65 \times 10^{-15} \text{ J}$ . Knowing the density of AuGa, its specific heat of about 41 J/mol.K was obtained.

### Supplementary References

1. B. Chen, Q. Gao, L. Chang, Y. B. Wang, Z. B. Chen, X. Z. Liao, H. H. Tan, J. Zou, S. P. Ringer, C. Jagadish, Attraction of semiconductor nanowires: An in situ observation. *Acta Mater.* **61**, 7166-7172 (2013).

2. C. J. Cooke and W. Hume-Rothery, The equilibrium diagram of the system gold-gallium *J. Less-Common Met.* **10**, 42-51 (1966).
3. R. P. Elliott and F. A. Shunk, The Au-Ga (gold-gallium) system. *Bull. Alloy Phase Diagr.* **2**, 356-357 (1981).
4. W. E. Stanchina, J. M. Whelan, Solubility of GaAs in Au-Ge eutectic melts. *Solid-state Electron.* **26**, 817-819 (1983).
5. C. H. Mueller, P. H. Holloway, R. G. Connell, The ternary phase diagram for Au-Ga-As using the flow chart technique. *MRS Proc.* **260**, 481 (1992).
6. J. Wang, Y. J. Liu, L. B. Liu, H. Y. Zhou, and Z. P. Jin, Thermodynamic assessment of the Au-Ga binary system. *CALPHAD.* **35**, 242-248 (2011).
7. O. Loebich, The optical properties of gold: A review of their technical utilization. *Gold Bull.* **5**, 2-10 (1972).
8. X. Huang, M. A. El-Sayed, Gold nanoparticles: Optical properties and implementations in cancer diagnosis and photothermal therapy. *J. Adv. Res.* **1**, 13-28 (2010).
9. M. A. Kats, R. Blanchard, P. Genevet, F. Capasso, Nanometer optical coatings based on strong interference effects in highly absorbing media. *Nat. Mater.* **12**, 20-24 (2013).
10. H. R. Philipp, H. Ehrenreich, Optical properties of semiconductors. *Phys. Rev.* **129**, 1550-1560 (1963).
11. Z. Gu, P. Prete, N. Lovergine, B. Nabet, On optical properties of GaAs and GaAs/AlGaAs core-shell periodic nanowire arrays. *J. Appl. Phys.* **109**, 064314 (2011).
12. H. Guo, L. Wen, X. Li, Z. Zhao, Y. Wang, Analysis of optical absorption in GaAs nanowire arrays. *Nanoscale Res. Lett.* **6**, 617 (2011).

13. S. Hu, C. Y. Chi, K. T. Fountaine, M. Yao, H. A. Atwater, P. D. Dapkus, N. S. Lewis, C. Zhou, Optical, electrical, and solar energy-conversion properties of gallium arsenide nanowire-array photoanodes. *Energy Environ. Sci.* **6**, 1879-1890 (2013).
14. S. I. Anisimov, B. L. Kapeliovich, T. L. Perel'man, Electron emission from metal surfaces exposed to ultrafast laser pulses. *Sov. Phys.-JETP* **39**, 375-377 (1974).
15. J. Tang, Coherent phonon excitation and linear thermal expansion in structural dynamics and ultrafast electron diffraction of laser-heated metals. *J. Chem. Phys.* **128**, 164702 (2008).
16. J. Chen, W. K. Chen, J. Tang, P. M. Rentzepis, Time-resolved structural dynamics of thin metal films heated with femtosecond optical pulses. *Proc. Natl. Acad. Sci. USA* **108**, 18887-18892 (2011).
17. C. L. Tien, A. Majumdar, F. M. Gerner, *Micro-scale Energy Transport* (Taylor & Francis, Washington D.C., 1998).
18. K. Fushinobu, A. Majumdar, K. Fujikata, Heat generation and transport in submicron semiconductor devices. *J. Heat Transfer* **117**, 25-31 (1995).
19. S. H. Lee, J. Lee, K. G. Kang, J. S. Lee, Three-temperature modeling of carrier-phonon interactions in thin GaAs film structures irradiated by picosecond pulse lasers. *J. Mech. Sci. Technol.* **20**, 1292-1301 (2006).
20. C. Kittel, *Introduction to Solid State Physics* (6<sup>th</sup> ed., Wiley, New York, 1986).
21. C. N. Bhandari, D. M. Rowe, *Thermal Conduction in Semiconductors* (Wiley, New York, 1988).
22. J. R. Meyer, M. R. Kruer, F. J. Bartoli, Optical heating in semiconductors: Laser damage in Ge, Si, InSb and GaAs. *J. Appl. Phys.* **51**, 5513-5522 (1980).
23. C. L. Collins, P. Y. Yu, Generation of nonequilibrium optical phonons in GaAs and their application in studying intervalley electron-phonon scattering. *Phys. Rev. B* **30**, 4501-4515 (1984).

24. P. Lugli, P. Bordone, L. Reggiani, M. Rieger, P. Kocevar, S. M. Goodnick, Monte Carlo studies of nonequilibrium phonon effects in polar semiconductors and quantum wells: I. Laser photoexcitation. *Phys. Rev. B* **39**, 7852-7865 (1989).
25. G. Benz, R. Conradt, Auger recombination in GaAs and GaSb. *Phys. Rev. B* **16**, 843 (1977).
26. D. Steiauf, E. Kioupakis, C. G. Van de Walle, Auger recombination in GaAs from first principles. *ACS Photonics* **1**, 643-646 (2014).
27. M. Neuberger, Handbook of Electronic Materials (IFI/Plenum, New York, 1970), Vol. 2.
28. J. S. Blakemore, Semiconducting and other major properties of gallium arsenide. *J. Appl. Phys.* **53**, R123-181 (1982).
29. H. Yao, S. L. Yau, K. Itaya, In situ scanning tunneling microscopy of GaAs (001), (111)A, and (111)B surfaces in sulfuric acid solution. *Appl. Phys. Lett.* **68**, 1473-1475 (1996).
30. S. Adachi, GaAs and Related Materials: Bulk Semiconducting and Superlattice Properties (World Scientific Publishing, Singapore, 1994).
31. J. Hohlfeld, S.-S. Wellershoff, J. Güdde, U. Conrad, V. Jähnke, E. Matthias, Electron and lattice dynamics following optical excitation of metals. *Chem. Phys.* **251**, 237-258 (2000).
32. J. Froemel, Gallium-based solid liquid interdiffusion bonding of semiconductor substrates near room temperature (Dissertation, Technische Universität Chemnitz, 2015).